Technichal University of Munich
Max Planck Institute for Extraterrestrial Physics
High-Energy Astrophysics

Bachelor's Thesis in Physics

Gamma-Ray Signatures of Time Variable Astrophysical Sources Observed with INTEGRAL

Gamma-Strahlung Signaturen von zeitlich variablen astrophysikalischen Quellen beobachtet mit INTEGRAL

Jakob Scheffel

May 11, 2018

Supervisor: Prof. Dr. Roland Diehl

Contents

List of Figures

List of Tables

1 Introduction

The goal of Astrophysics is learning about phenomena that occur outside the Earth' atmosphere and understanding which objects and processes are involved. Because most of the objects of interest find themselves in great distance to Earth, carrying out observations always becomes a challenge.

In order to learn about the properties of astrophysical objects, one can not rely on manipulating a setup as is done in common experiments on Earth, but has to observe phenomena from outside and work with the information that can be obtained from such observation. Much cosmic information is transported by electromagnetic radiation in a great variety of wavelengths - from radio radiation through the optical regime up to X-ray and γ-ray energies.

In the γ-ray regime, one instrument to obtain information is the International Gamma Ray Astrophysics Laboratory (INTEGRAL). Due to the high optical depth for γ-rays of the earth' atmosphere, such observations have to be carried out outside of it, on a satellite such as INTEGRAL. Gamma radiation can hold a lot of information about processes under extreme conditions. Thus, e.g. when nuclei decay, they usually end up in an excited state and then de-excite by the emission of photons carrying characteristic energies, mostly in the γ-range. This can lead to conclusions about the chemical elements an object consists of. Other processes that create γ-radiation are bremsstrahlung from charged particles or matter-antimatter-annihilation processes (e.g. of electrons and positrons) which also radiate at specific energies.

Most objects treated in astronomy have built up over millions to billions of years, making it difficult to observe significant changes within these processes, because they evolve very slowly. Shorter processes in astrophysics are called *transients*. These phenomena include e.g. Supernovae, Novae, Solar flares or gamma-ray bursts. Such transients can be observed i.a. in γ-radiation data from INTEGRAL. From γ-radiation data one can learn about what certain objects (e.g. the Sun, stars) consist of and from variations in γ-ray data one can conclude about how they evolve in time. Because γ-radiation is particularly produced in high energy processes, e.g. nuclear reactions, that occur during all of the aforementioned transients, a lot of knowledge about processes and mechanisms can potentially be drawn from looking at the γ-ray signatures of astrophysical transients.

The Spectrometer on board INTEGRAL (SPI) consists of Germanium detectors, measuring photons in the energy range from 20 keV to 8 MeV. For each event it measures the energy deposited in the detector and the incident time, so light curves as well as spectra can be obtained from it.

Because SPI measures single photons in a great energy range, the data obtained from SPI is dominated by background, meaning only few of the photons measured carry information about the investigated phenomena. Thus, to obtain knowledge from the data measured, it is necessary to determine which photons belong to the background and which photons are part of the sky that one wants to observe.

In this thesis, transient γ-ray sources, as observed with SPI spectrometer, are analyzed in a way that does not depend on a specific model. This shall be achieved by use of the Bayesian block method which is based on Poisson statistic in combination with Bayesian inference. This method can be operated almost unbiased and allows an investigation of the behavior of rapidly changing astrophysical sources by spectral analysis.

In chapter 2 an overview over the behavior of γ-radiation in general will be given, starting with the description of processes which create γ-radiation. To understand the behavior and the possible ways of measuring such radiation, its ways of interacting with matter shall be described in the following. In the third chapter, the INTEGRAL mission will be described, paying particular attention to the SPI spectrometer and its operating principle. After this, some astrophysical transient sources shall be characterized with particular emphasis on radiation events in the γ-regime. In the chapter following thereafter, some methods used for the analysis of SPI data will be described.

After that, the theoretical basis is discussed in enough detail to continue with the investigation of actual SPI data. The statistical methods described in chapter 5 will be applied to such data, performing an analysis with the Bayesian block method and conducting a spectral analysis after that. In Chapter 7, the observations made will be discussed and put into context.

2 Gamma-Ray Production and Interaction of Gamma-Rays with Matter

Gamma-radiation is a form of electromagnetic radiation, that is characterized by photon energies of $E_\gamma > 100keV$. They are produced in high energy processes, e.g. nuclear reactions. In the following, three processes of γ-ray production shall be explained: The production through radioactive decay, annihilation of matter with antimatter and particle acceleration. After that, its dominant interaction mechanisms with matter shall be discussed.

2.1 Production of Gamma-Radiation

2.1.1 Radioactive Decay

Radioactive decay occurs in atomic nuclei, that are unstable, which means they consist of an amount of nuclear particles of such quantity, that the binding energy "fails" to hold them together. In order to stabilize, particles are spontaneously emitted out of the nucleus. After such emission, the nucleus may remain in an excited state, before it emits a γ-photon for de-excitation. In some cases the radioactive decay does not stop after that, because the daughter nucleus may still be unstable and thus keeps decaying.

One form of radioactive decay is the emission of an α-particle (α-decay). The α-particle consists of two protons and two neutrons and is therefore a ^{4}He nucleus. The α-decay process can be written schematically as

$$ {}^{A}_{Z}X \rightarrow {}^{A-4}_{Z-2}Y + {}^{4}_{2}\alpha $$

where X is the species of the mother nucleus and Y the species of the daughter nucleus, A being the mass number and Z being the atomic number. The energy released in an α-decay stems from the nuclear binding energy of core particles which is set free by the separation of the daughter nucleus and the α-particle. It appears solely in kinetic energy of the α particle and the daughter nucleus. Due to momentum conservation, both particles must have equal but opposite momenta, leading to well defined energies after decay (Knoll 2011). An example for the α-decay process is shown in Figure 2.1.

Another radioactive decay process is the β-decay, in which either electrons (e^-) or positrons (e^+) are emitted. The β^--decay proceeds according to the scheme

$$ {}^{A}_{Z}X \rightarrow {}^{A}_{Z+1}Y + e^- + \bar{\nu}_e, $$

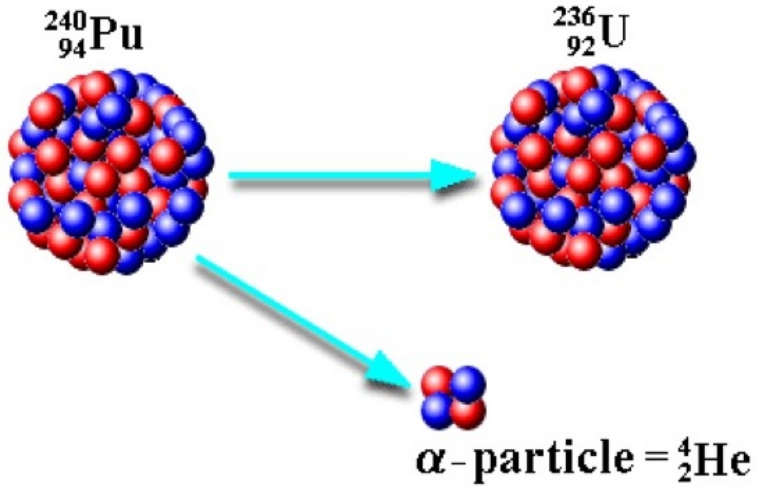

Figure 2.1: The α-decay of $^{240}_{94}$Pu to $^{236}_{92}$U. From Garland 2018.

where e^- is an electron and $\bar{\nu}_e$ is an electron-anti-neutrino. In detail, a neutron within the atomic nucleus decays into a proton and an electron. In order to conserve lepton number and flavor, a electron-anti-neutrino has to be emitted as well. Accordingly, the β^+-decay is described as

$$^A_Z X \rightarrow ^A_{Z-1} + e^+ + \nu_e.$$

Here a proton inside an atomic nucleus decays into a positron (e^+) and a neutron, while emitting an electron-neutrino. In β-decays, the mass number A is conserved and only the atomic number Z changes. Because in both β-decay processes there are three decay products, the energy is not discrete as is the case with the α-decay. The decay energy spectrum of the β-decay is a continuum (Knoll 2011).

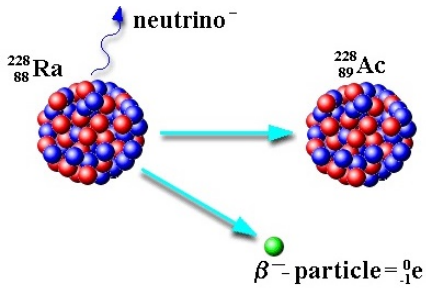

Figure 2.2: The β^--decay of $^{228}_{88}$Ra to $^{228}_{89}$Ac. From Garland 2018.

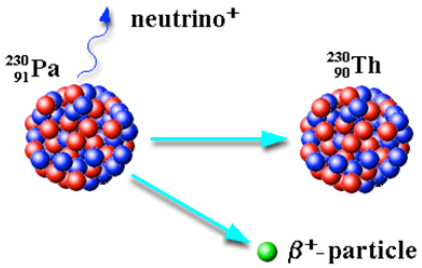

Figure 2.3: The β^+-decay of $^{230}_{91}$Pa to $^{230}_{90}$Th. From Garland 2018.

In Figure 2.2 and 2.3 examples for the β-decay can be seen.

After one of the decays described above, the nucleus is often left in an excited state. As can be seen in Figure 2.4, a nucleus can then be de-excited by the emission of electromagnetic radiation, which typically is of the order of a few 100s of keV to 10s of MeV and hence γ-radiation (Knoll 2011).

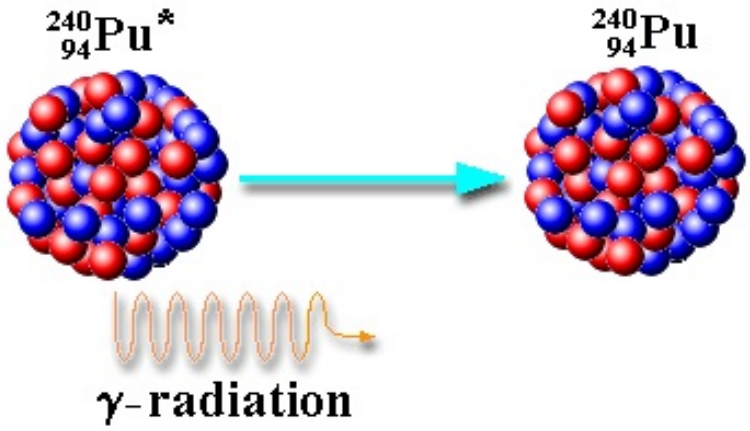

Figure 2.4: The de-excitation of $^{240}_{94}$Pu* under emission of a 160.3 keV γ-photon. From Garland 2018.

2.1.2 Matter-Antimatter Annihilation

The standard model of particle physics states, that to every particle, there is an anti-particle which has the same spin and mass, but opposite charge. The anti-electron therefore is the positron. When an electron and a positron interact with each other, they can form a bound quantum state, that shares similar properties to hydrogen and is called *positronium*. The positronium can exist in one of two states: If the spins of the e^- and e^+ are anti-parallel, one speaks of *para-positronium*, which has an average lifetime of 0.125 ns, before it decays in two photons. If the spins are parallel one speaks of *ortho-positronium*, which has an average lifetime of 142 ns, before it decays into three photons, each having an energy of at most 511 keV. If no bound state is formed, an e^- and e^+ can annihilate directly into two photons, each having an energy of 511 keV in the rest frame. Similar annihilation processes take place with different particles (e.g. proton and anti-proton) as well, where the characteristic emission energies vary according to the rest masses of the particles (Martin and Shaw 1997).

2.1.3 Particle Acceleration

Particles which carry a charge, such es electrons, build up a Coulomb field around them that consists of radial field lines. If the particle is accelerated, the electric field lines will become perturbed which due to the Lorentz force leads to energy loss of the charged particle in the form of electromagnetic radiation. From Coulomb's law and Maxwell's equations one can derive the *Larmor formula* to calculate the energy loss via radiation by an accelerated particle:

$$\frac{dE}{dt} = \frac{q^2 a^2}{6\pi\epsilon_0 c^3}, \tag{1}$$

where q is the particle's charge, a is the acceleration and c is the speed of light (Courvoisier 2013). According to equation (1), for sufficiently high accelerations, photons in the γ regime can be emitted.

2.2 Interaction of Gamma-Rays with Matter

If one wants to measure γ-rays, one needs to understand the interaction of electromagnetic radiation with matter. Unlike optical photons, γ-rays interact with matter in different ways, depending on their energy. There are many possible interaction mechanisms for γ-rays in matter, only three of which play a major role in radiation measurement: The *photoelectric effect*, *Compton scattering* and *Pair production*. Generally all these processes lead to energy being transferred from a γ-photon to electrons. (Knoll 2011)

2.2.1 Photoelectric Effect

Low energy photons interact with matter mostly by the photoelectric effect, which has first been described by Einstein 1905. It can only occur with an electron that is bound in an atom, but does not work with free electrons. During the interaction of the photon with the absorber atom, the photon "disappears" completely, being replaced by a *photoelectron*, which is ejected by the absorber atom and which has a kinetic energy of

$$E_{e^-} = h\nu - E_b, \tag{2}$$

where ν is the frequency of the absorbed photon and E_b is the binding energy of the photoelectron before interaction. When looking at γ-photons of a few keV energy, the electron carries off most of the original photon energy.

The absorber atom is left ionized, so in a next step, either an electron is captured from the medium or the electrons from other shells of the atom are rearranged to fill the empty spot, which leads to another photon being

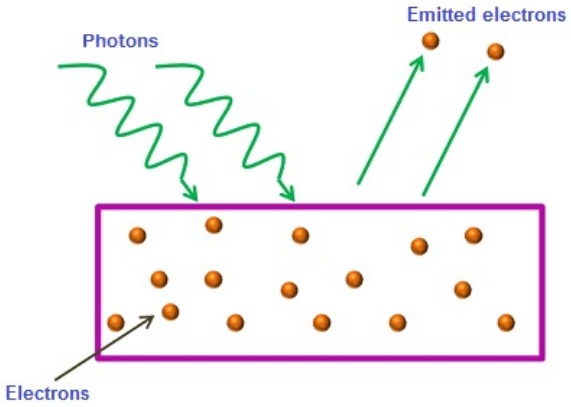

Figure 2.5: The photoelectric effect: Electrons are being ejected out of the material after the interaction with photons. From Shaik 2018.

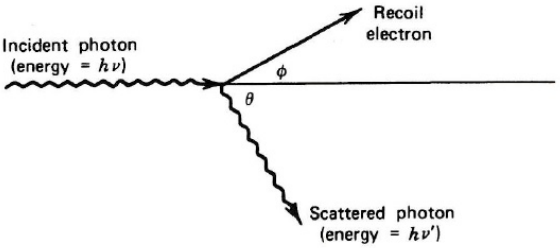

Figure 2.6: The general principle of (elastic) Compton scattering. From Knoll 2011.

emitted. A schematic view of the photoelectric effect is shown in figure 2.5. This is the predominant mode of interaction for γ-rays of relatively low energy and is favored by absorber materials with high atomic number Z (Knoll 2011).

2.2.2 Compton Scattering

For photons of higher energies, the main interaction process with matter is Compton scattering. It takes place between γ-radiation of high energy and electrons, which are generally considered to be free (taking the binding energy into account does not make much of a difference in the energetic regions of Compton scattering). The basic principle of this process is elastic scattering as is shown in Figure 2.6. From the conservation of energy and momentum it follows that

$$h\nu' = \frac{h\nu}{1 + \frac{h\nu}{m_0 c^2}(1 - cos(\theta))} \tag{3}$$

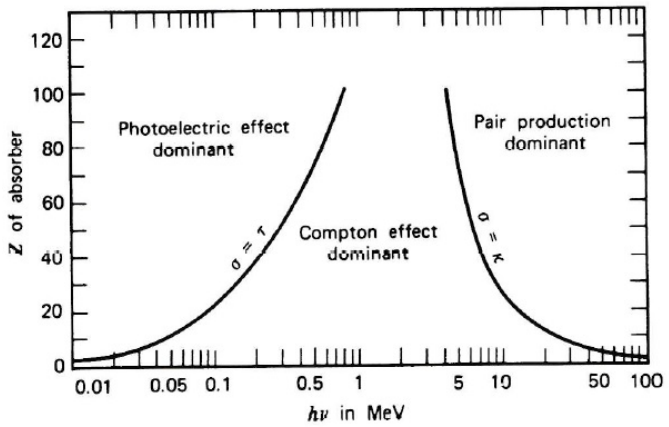

Figure 2.7: The relative importance of the three major types of gamma-ray interaction. The lines show the values for Z and $h\nu$ for which the two neighboring effects are just equally probable. From Knoll 2011.

where m_0 equals the rest mass of the electron (511 keV/c^2). Thus the interacting photon always keeps some of its energy, and is not completely absorbed as in the above described photoelectric effect. The probability of Compton scattering occurring rises, when the atomic number of the interacting material increases, because with higher Z there are more electrons that are available for interaction (Knoll 2011).

2.2.3 Pair Production

The process of pair production starts when photons reach energies larger than 1.02 MeV which is twice the rest mass of an electron. With photon energies above this threshold the probability of pair production occurring grows as well. During pair production, a high energetic γ-photon which passes the Coulomb field of an atomic nucleus splits up into a pair of an electron and a positron. The energy above the threshold of 1.02 MeV goes into the kinetic energy of both produced particles. As the positron slows down while passing through the material it will eventually annihilate with an electron from the material, ultimately leading to two γ-photons being emitted, each having an energy of 511 keV and flying in opposite directions.

In Figure 2.7 one can see the relative importance of the three interaction processes described above with respect to the photon energy and the atomic number Z of the interacting material.

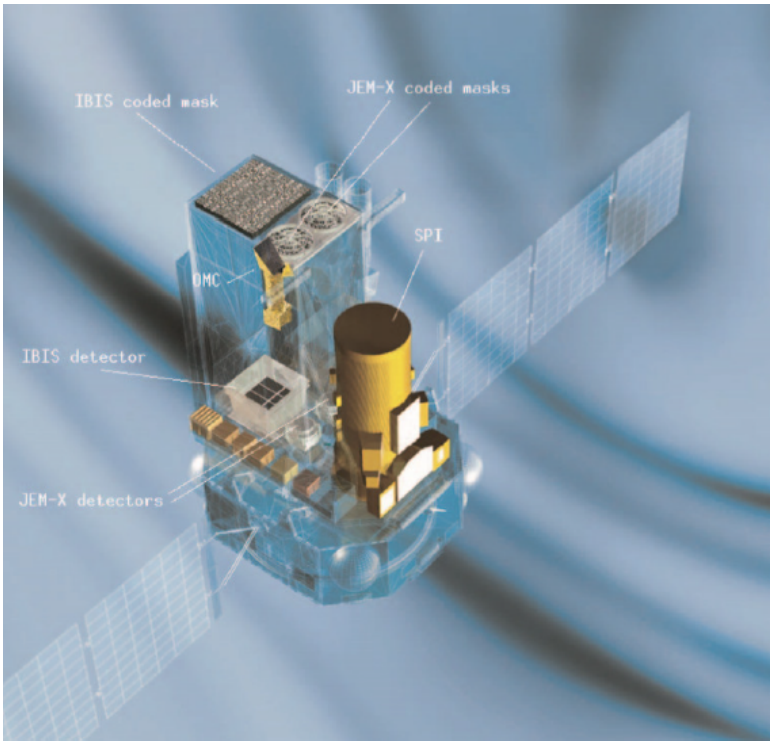

Figure 3.1: An impression of the INTEGRAL satellite. It has dimensions of $5 \times 2.8 \times 3.2$ m. From Kretschmar et al. 2005.

3 The INTEGRAL Mission

3.1 The Satellite

The International Gamma Ray Astrophysics Laboratory (INTEGRAL) is a satellite that was launched in October 2002 and that is equipped with different instruments for the measurement of mainly X-ray and γ-ray photons. It is in a 72-hour-orbit around Earth, with a height of perigee of 9.000 km and a height of apogee of 154.000 km (Winkler et al. 2003). The high apogee ensures that for a long time per orbit scientific observations can be carried out without disturbance by radiation trapped in the Earth's magnetic field. When approaching Earth and its radiation belts, measurements are stopped at an altitude of 60.000 km and resumed at an altitude of 40.000 km when leaving the radiation belts. Thus, more than 80% of the orbit time can be used for scientific observations (Kretschmar et al. 2005).

The two main instruments on INTEGRAL are the Imager on board the INTEGRAL satellite (IBIS), with a field view of $9° \times 9°$ measuring photons between 15 keV and 10 MeV, and the Spectrometer on INTEGRAL (SPI),

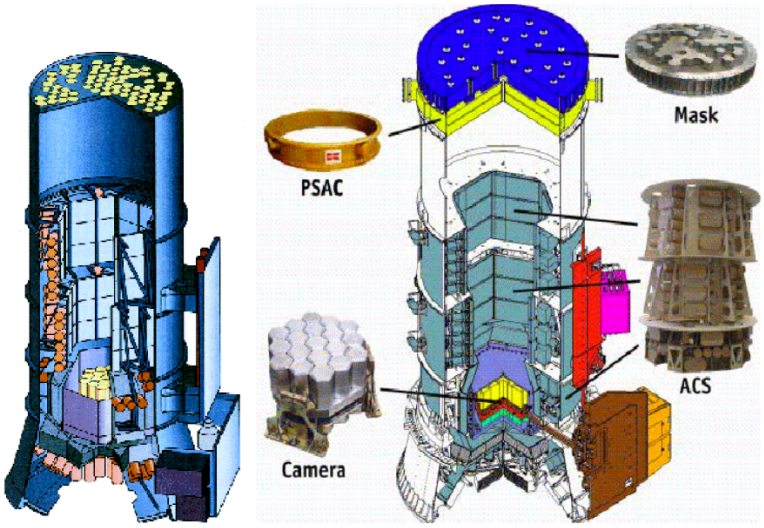

Figure 3.2: SPI instrument on INTEGRAL. From Diehl et al. 2017.

with a field view of $16° \times 16°$, mesuring photons between 20 keV and 8 MeV. The SPI instrument will be described in detail below.

Besides the two main instruments, INTEGRAL carries two monitoring instruments, which are the Joint European X-Ray Monitor (JEM-X) in the energy range from 3 keV to 35 MeV and an optical monitor camera (OMC) observing wavelengths between 500 and 600 nm.

The goal of the INTEGRAL mission is the examination of high energetic phenomena that can be investigated by γ-ray spectroscopy. SPI and IBIS allow the examination of large energy ranges, positioning of γ-ray sources and gaining information about the chemical composition of different scientific objects by examination of the γ-ray line spectrum. This is also used to study astrophysical transients and corresponding nucleosynthesis processes. An impression of the INTEGRAL satellite can be seen in Figure 3.1.

3.2 The SPI Instrument

The *Spectrometer on INTEGRAL* (SPI) is a coded mask telescope. The data used in this thesis was taken with SPI. The SPI instrument is outlined in Figure 3.2.

It consists mainly of three parts: The Germanium detector camera, a mask made of tungsten that shields parts of the viewing field, and an anti-coincidence detector system (ACS) which surrounds the composition. The purpose of the ACS is to filter events originating from prompt cosmic-ray interactions by the use of BGO scintillators. The registration of SPI events by the Ger-

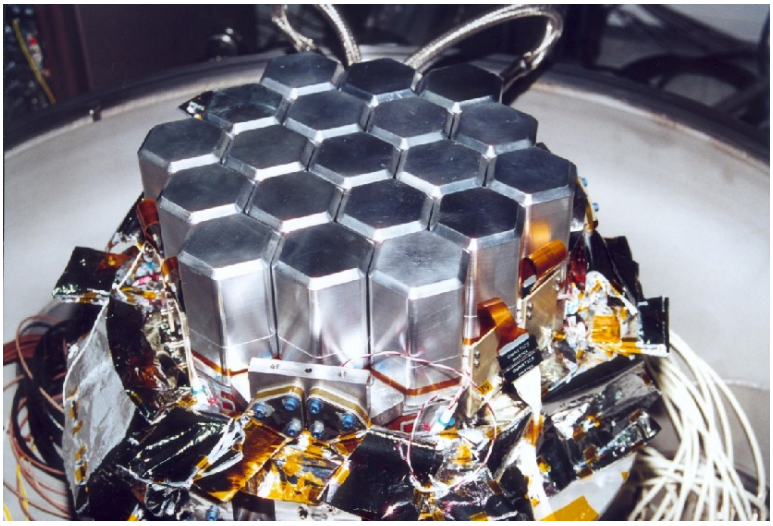

Figure 3.3: The 19 Germanium detectors on SPI forming the γ-ray camera. From Dubath et al. 2005

manium detectors is disabled for 725 ns when the ACS is triggered. In this way, γ-ray-events can be filtered from events outside the field of view. The heart of SPI, the Ge detector camera, is shown in Figure 3.3. It consists of 19 Germanium detectors with a hexagonal shape. Each detector has a side length of 32 mm, a height of 69.42 mm, an external diameter of 60.65 mm, a distance of 56.04 mm from one flat side to the other and the centers of neighboring cells are 6 cm apart from each other. The hexagonal shape optimizes the use of space in the instrument and therefor reduces its needed volume. The Ge detector scheme is shown in Figure 3.4. The Ge detectors are cooled to 85 K to reduce the effect of radiation damage on the material and to increase the sensitivity and therefor the resolution of the Ge detectors (Diehl et al. 2017; Kretschmar et al. 2005; Dubath et al. 2005).

The SPI mask is mounted 1.71 m above the Germanium detector camera. It is made from tungsten, has a mass of approximately 140 kg and consists of 127 hexagonal pixels, 64 of which are transmissive for γ-radiation and 63 of which are opaque to the radiation within SPI's energy range. The pattern is arranged in a circle of 72 cm diameter and presents a 120° rotational symmetry. A photo of the mask is shown in Figure 3.5 (Dubath et al. 2005). The mask shielding leads to an intensity distribution among the Ge detectors, that makes it possible to code the incoming γ-rays within the Field of View (FoV) of SPI. A schematic shadowgram of the Ge detector camera in different viewing angles to a point source is shown in Figure 3.6. With help of this shadowgram, the location of γ-ray point sources can be retraced by the direction they arrive from with an angular resolution of 2.5° (Dubath et al. 2005; Kretschmar et al. 2005).

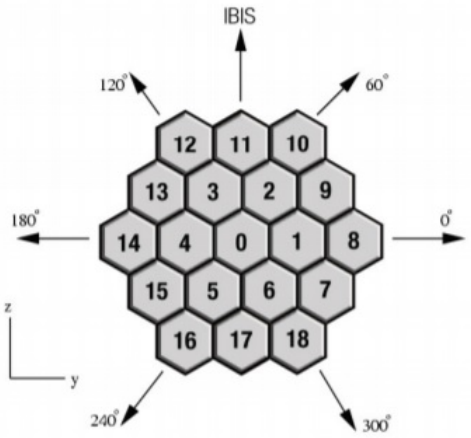

Figure 3.4: The structure of the Germanium detectors on INTEGRAL's SPI (Diehl et al. 2017)

Figure 3.5: The tungsten mask shielding the Germanium detector camera. From Dubath et al. 2005.

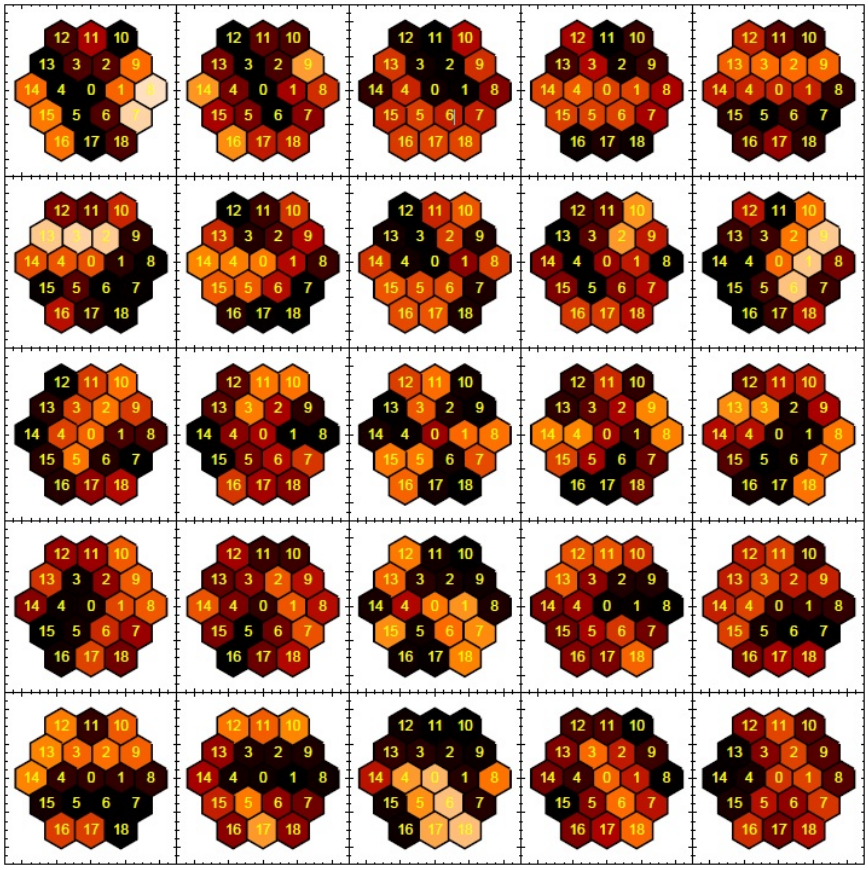

Figure 3.6: The Shadowgrams of the 19 Ge detectors for a point source on axis during 25 pointings, between two of which the telescope has been re-orientated in steps of 2.1°. The detectors are color-coded from white/yellow (full exposure) to black (no detected radiation). From Diehl et al. 2017.

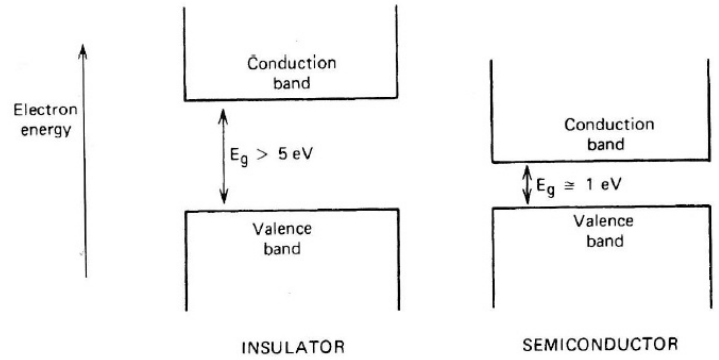

Figure 3.7: The band structure for electron energies in insulators and semiconductors. From Knoll 2011.

Usually, the satellite stares at a particular position for approximately 30 minutes, and is reorientated by steps of 2.1° thereafter. The interval of the satellite staring at one particular position is called a *pointing*, the reorientation time is called a *slew* (Winkler et al. 2003).

3.3 Operating Principle of Germanium Detectors

Germanium detectors belong to the group of semiconductor diode detectors. To understand the working principle of Ge detectors, the most common model to describe the physical process, the band model, is introduced. A simplified representation of this model is shown in Figure 3.7. The lower band, called *valence band*, consists of electrons which are located in the outer atomic shells and that take part in the covalent bonding within the crystal lattice. The next band of higher energy is called *conduction band*. There, the electrons are able to move through the crystal and therefore contribute to the electrical conductivity of the material. Those two bands are separated by an energy gap, the size of which classifies the material as semiconductor, insulator or conductor (metal). The number of electrons within a crystal fills up every available site in the valence band. Therefore, if no excitation takes place, the valence band is completely filled, whilst the conduction band remains completely empty. Because only energy bands that are occupied, but not completely full contribute to electrical conductivity, in this case, no electrical conductivity is measured (Knoll 2011).

Due to thermal energy, there is a possibility for an electron to get out of the valence band, be elevated through the gap into the conduction band. Due to this excitement, an electron in the otherwise empty conduction band is created, and also leaves a vacancy (*hole*) in the otherwise full valence band. This combination is called an *electron-hole-pair*. If an electric field

is applied to the setup, the electron, being negatively charged, will move under its influence. The hole left by the electron, compared to the before uncharged state, has a net positive charge, and will therefor also move in an electric field, which can be observed as conductivity. The probability for a thermally generated electron-hole-pair per unit time is given by

$$p(T) = CT^{3/2} \exp\left(-\frac{E_g}{2k_B T}\right) \tag{4}$$

where T is the absolute Temperature, E_g is the energy gap between the valence and conductivity band, k_B is the Boltzmann constant and C is a material-dependent proportionality constant. In order to reduce the probability for thermally generated electron-hole-pairs, Ge detectors are cooled to low temperatures (Knoll 2011). The Ge detectors on INTEGRAL's SPI are cooled to 85 K (Kretschmar et al. 2005).

In order to use Germanium as detector material, electron-hole-pairs are also created when a particle deposits energy in a semiconductor detector. When an electric field is applied to the detector, the electron and the hole will both drift in opposite directions, constituting two electric currents, which will persist until the charge carriers are collected at the boundaries. Because the holes are less mobile than the electrons, the current of holes is less intense, but lasts longer than the electron current. Therefore, in order to measure the actual energy being deposited by the detected particle, both currents must be integrated completely (Knoll 2011).

The voltage should be sufficiently high, to accelerate the charge carriers to high velocities, thereby reducing the collection time of the detector (Knoll 2011). The Germanium detectors on INTEGRAL's SPI usually work with a voltage of 4 kV, resulting in 102.4 μs time accuracy and a spectral resolution of 3 keV at an energy of 1.7 MeV (Vedrenne et al. 2003).

The ability to measure single photons with the good time and energy resolution of SPI constitute its suitability to investigate rapidly changing γ-ray sources and analyze their spectra in great detail.

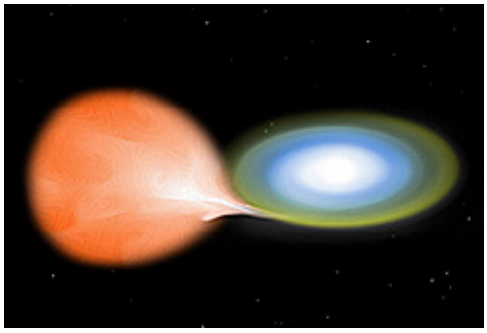

Figure 4.1: An artist's impression of the mass accretion in a binary system, leading to a Nova. From NASA 2018b.

4 Astrophysical Transient Sources

The word *"transient"* originates from the Latin word *"transire"* which translates as *"to go by"*. Following this interpretation, astrophysical transient sources are objects or events, that take place on an astronomical scale, that *go by*, ergo are not observed persistently (Bone 1999). There is a great variety of different transients, such as novae, supernovae, radioactive galactic nuclei, black holes, solar flares and gamma ray bursts. In the following, the transients that are of particular interest for high-energy observations, especially with SPI, will be described in detail. Such transients are gamma-ray bursts, novae, supernovae and solar flares. For all these transients, γ-ray signatures in different energy regions have been observed, and characteristics have been observed within the spectra of such transients.

4.1 Novae

The word *"Nova"* originates from the Latin *"stella nova"* ("new star") and stems from Tycho Brahe (Brockhaus 2006). It describes the observation of an explosive nuclear reaction on the surface of a *white dwarf* (WD) under degenerate conditions (Shore 2012).[1] This reaction is a consequence of the accretion of hydrogen-rich material onto the WD's surface in a binary system as is shown in Figure 4.1. Over time, the gravitational pressure of this accretion layer heats the inner layers, such that the electrons degenerate eventually and the temperature exceeds 10^8 K. Consequently, nuclei start to capture a proton, forming a β^+-unstable isotope (e.g. ^{15}O) (Bode and Evans 2012; Shore 2012; Gehrz et al. 1998).

Once the inner layers of the accreted matter become hot enough, a *thermonuclear runaway* is ignited, which means hydrogen burning is taking place,

[1] "Degenerate" means, that the Fermi energy of leptons exceeds the thermal energy

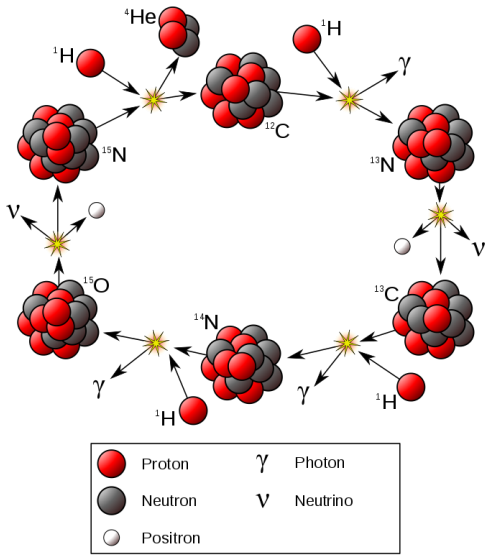

Figure 4.2: The principle of the CNO-cycle. From Witte 2018.

starting with the proton chain ($p^+ + p^+ \rightarrow {}^2_1\mathrm{H} + e^+ + \nu$; Schatzmann 1958), and subsequently get to the CNO-cycle. The working principle of the CNO-cycle is presented in Figure 4.2. It starts (at the top of the picture) with a ^{12}C from the stellar core capturing a proton, thus producing a β^+-instable ^{13}N and a γ-photon. The Nitrogen then emits an e^+ and a neutrino, leaving a ^{13}C which again captures a proton, creating a ^{14}N under emission of another photon. The Nitrogen captures another proton, producing a ^{15}O which then decays by emission of an e^+ and a neutrino, thus leaving behind a ^{15}N. After capturing another proton, this will carry out an α-decay, therefor emitting an $^4_2$He, leaving the ^{12}C behind, so the circle can start once more (Bode and Evans 2012). This cycle, particularly the β^+-decays in it, fuels the energy to heat up and expand the less dense outer layers of the star. Due to the heat, heavier nuclei up to atomic numbers 40 can be formed as well. Of certain interest for γ spectroscopy are especially ^{22}Na and ^{7}Be due to their strong, mono-energetic emission lines. Other β^+-unstable isotopes can also be measured through the 511 keV annihilation line (Siegert et al. 2018).

Subsequently, due to the rapid increase in temperature as a consequence of nuclear fusion and the decays described above, material between 10^{-5} and 10^{-4} $M_\odot$ is ejected at velocities of hundreds to thousands of km per second (Bode and Evans 2012) .

To investigate the time component of a transient source, one usually observes its lightcurve. That is the counts measured at the detector as a function of

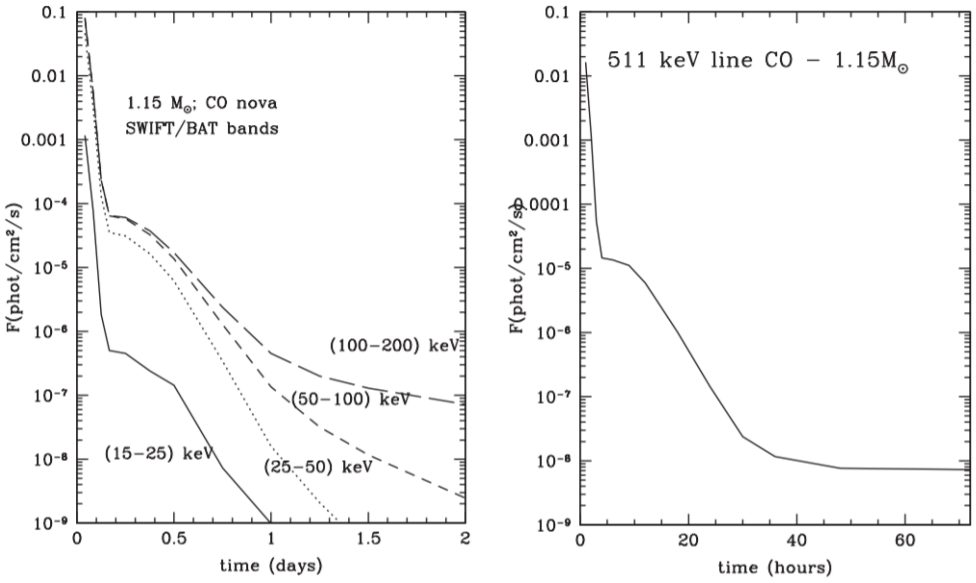

Figure 4.3: The lightcurve for various spectral lines of a nova with mass 1.15 $M_\odot$ (left) and the lightcurve for the 511 keV line for a nova of 1.15 $M_\odot$. From Hernanz 2013.

time. From looking at the lightcurves in Figure 4.3 and the corresponding spectra in Figure 4.4, one can see, that the timescale on which Novae are observed is approximately in the magnitude of 1-3 days, where the main observation is made over only several hours (Hernanz 2013).

When observing Novae, it is expected to find a strong signal from the 511 keV spectral line. Therefore, the 500-520 keV energy band is of particular interest when observing novae.

4.2 Supernovae

A supernova (*SN*) occurs at the end of a star's life. When the nuclear fusion in its core terminates, the thermal energy, that used to counterbalance the gravitational pressure, drops, such that the star explodes (Hanslmeier 2014). Supernovae can be classified depending on the mass of the progenitor star. Stars of low masses usually end as a White Dwarf. These may then explode in Supernovae of Type Ia. Moderate and high mass stars end up in a Supernova of type Ib/c or II. The general classification is based on whether the spectrum of the supernova (thus their ejecta) contains Hydrogen (Type II) or not (Type I) (Panagia 2000). Type II SNe are produced by the collapse of a star's core, which requires a mass of preceding star of 10-100$M_\odot$. These SNe are also called Core Collapse Supernovae (*CCSNe*) (Hanslmeier 2014).

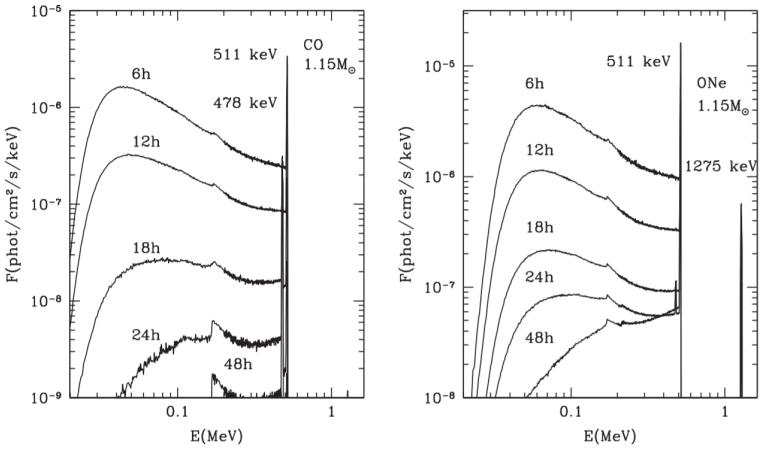

Figure 4.4: The spectra of two Novae of mass 1.15 $M_\odot$ at different epochs after T_{peak}. From Hernanz 2013.

SNe of Type I are found to contain two subclasses which are called Ia and Ib/c (Panagia 1985). The subclassification is based on the presence (Ia) or absence (Ib/c) of a strong Si^+ absorption line at $\lambda = 6150$ $\mathring{A}$. Type Ib SNe also include He-lines, which cannot be found in the spectra from SNe of type Ic (Janka 2012). Type Ia SNe can be found in any galaxy, while SNeIb/c and CCSNe are usually found in spiral or irregular galaxies which leads to the indication that the latter belong to considerably young progenitor stars (less than 100 Million years of age) (Panagia 2000).

The kinetic energies set free during SNe can reach up to $\sim 10^{51}$ erg and are believed to stem from the gravitational energy set free during the collapse towards a compact object, or its nuclear energy, released in explosive reactions. For SNe of type II, compact objects (such as neutron stars) can be found in the remnants of the SN, while after SNe of Type Ia no such compact object is found within the remnants, which leads to the suggestion, that the progenitor stars of Type Ia SNe are white dwarfs (WDs) consisting of Carbon and Oxygen (Roepke 2008).

Usually, when the nuclear fusion in a WD stops, the WD cools over time. Yet it is believed that WDs that are part of binary systems can end in SNe Ia, after the WD accretes matter from another star (e.g. a main sequence star) by which the WD reaches the *Chandrasekhar mass* ($M_{Ch} \approx 1.4$ $M_\odot$) which is the critical mass for enabling a SN of type Ia. This would explain the unusual uniformity in intensity, spectrum and light curves of type Ia SNe (Roepke 2008). The gravitational pressure within the WD is increased by the accreted mass such that nuclear fusions (e.g. of carbon nuclei, Roepke 2008) inside the core are ignited, leading to a thermonuclear runaway (Janka 2012). This leads to a rapid increase in thermal energy which is then blowing

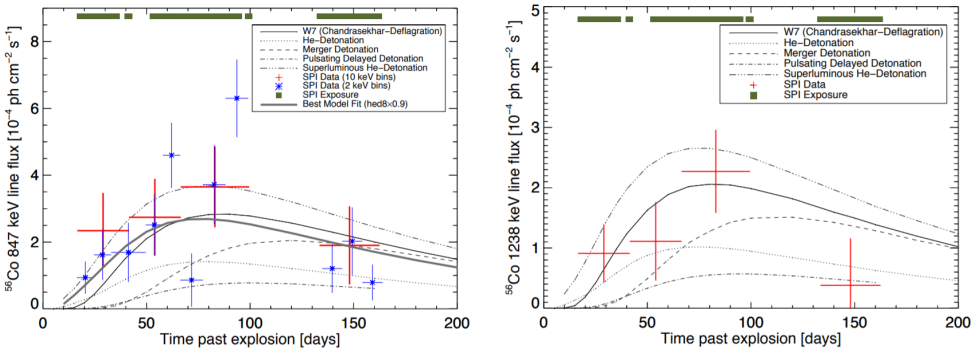

(a) The lightcurve for the 847 keV line.

(b) The lightcurve for the 1238 keV line.

Figure 4.5: The lightcurves of the two de-excitation lines of ^{56}Co as observed in SN2014J. Both plots have been taken from Diehl et al. 2015.

the star up. During this process $\approx 0.6 M_{\odot}$ of radioactive ^{56}Ni is produced (Panagia 2000) which decays to ^{56}Co by electron capture with a half-life of 6 days (Piluso, Wells, and McDaniels 1966), and again decays to ^{56}Fe by electron capture with a half-life of 77 days. (Kienle and Segel 1959) These decays produce excited nuclei whose de-excitation can be measured with the help of Gamma telescopes. The emission lines expected for the de-excitation of ^{56}Co lie at 847 keV and 1238 keV and have been measured by INTEGRAL (Diehl et al. 2015). The exact explosion mechanism (e.g. does it start at one central spot or in multiple sparks with stochastic distribution?) of type Ia SNe is yet object of research (Roepke 2008).

Figure 4.5 shows the lightcurves for the de-excitation of ^{56}Co. From the plots one can see, that for SNe the timescale is of the magnitude of several weeks to months, which means a much greater timescale than e.g. Novae (Diehl et al. 2015).

For SNe of type Ib/c and II the general explosion mechanism is not the thermonuclear runaway but the implosion of the stellar core. This process starts when the hydrogen burning in the stellar core gets exhausted, the star therefore leaves the main sequence (MS) and thus the stellar evolution process speeds up. The nuclear burning becomes more efficient due to the larger fusing nuclei. Once the central temperature of the star rises above $T_c \sim 10^9 K$, e^+e^- pairs become abundant and the energy loss by neutrino-antineutrino-pairs being produced accelerates. This energy drain happens at the expense of gravitational binding, leading to a contraction of the stellar core (Janka 2012).

The stellar core eventually enters the regime of electron degeneracy, stabilizing the star by lepton degeneracy pressure, such that it will cool at

approximately constant density (Panagia 2000).

If, however, the progenitor star exceeds a birth mass limit of $M_* \gtrsim 8$ $M_\odot$, the lepton degeneracy pressure does not suffice to counter the gravitational pressure of the collapsing stellar core. Then the stellar core keeps collapsing, until it reaches nuclear densities ($\rho \gtrsim 2.7 \cdot 10^{14} \frac{g}{cm^3}$), at which point the collapse abruptly stops due to the phase transition to homogeneous nuclear matter. This means a sudden increase in pressure, because of short-range forces between nucleons. The outer layers bounce back when hitting the solid surface of the dense stellar core and leave behind only the high density inner region of the progenitor star which now forms a neutron star (*NS*) (Janka 2012). As a consequence of the nuclear fusions that took place before the final collapse, the SN remnant contains several radioactive isotopes which can be measured, e.g. by INTEGRAL (Diehl et al. 2017).

If the birth mass exceeds $M_* \gtrsim 40 M_\odot$, the collapse does not end when nuclear density is achieved, but the stellar core keeps collapsing, until its radius falls below the *Schwarzschild-Radius*. The Schwarzschild-Radius is the radius below which the escape velocity exceeds the speed of light. By the formula for the escape velocity one can easily derive the Schwarzschild Radius:

$$v_{escape} = \sqrt{\frac{2GM}{r}} \Rightarrow r_s = \frac{2GM}{c^2}, \tag{5}$$

where G is the gravitational constant and M is the object mass. The remaining object is then called a Black Hole (*BH*) (Kutner 2003).

4.3 Solar Flares

The Sun has a radius of $6.959 \cdot 10^8$ m, a mass of $1.98 \cdot 10^{30}$ kg, a surface temperature of ∼5777 K and consists mainly of hydrogen and helium. In the Sun's core, protons fuse into Helium, which dominantly happens via the following mechanism: (Hanslmeier 2014)

$$4p^+ \rightarrow {}^4\mathrm{He} + 2e^+ + 2\nu_e$$

This reaction generates most of the energy that is emitted by the sun and takes place in its core (Garcia et al. 2007). Outside the core is the Sun's radiative zone, which ends at approximately 70% of the radius (Garcia et al. 2007). The radiative zone gets its name from the primary method of energy transport within it, which is radiation. Thus photons from the nuclear reactions are transported outwards. After passing through, the energy is transmitted to the convection zone, where energy is transported by convection. The convection zone reaches from the edge of the radiation zone up to the solar surface. Here, some atoms begin to form, which due to the radiation from the inner parts start "boiling" or convecting immediately, such

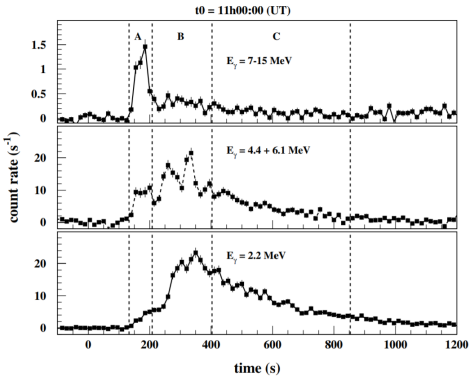

(a) The lightcurves in various energy bands of a solar flare.

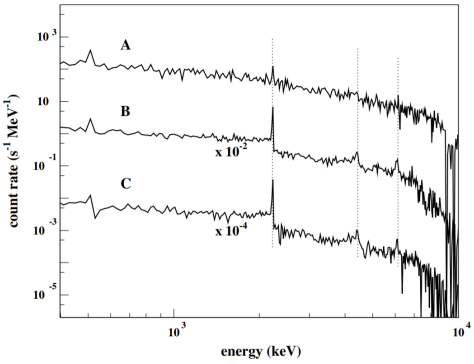

(b) The spectra of the solar flare signal over the intervals A, B and C.

Figure 4.6: This Solar flare was observed by INTEGRAL on October 28$^{\text{th}}$, 2018. Both plots are taken from Kiener et al. 2005.

that they start "flowing" towards the solar surface, while "cooler" parts flow back down towards the edge of the radiative zone (NASA 2018c). By these fluctuations of charged particles, magnetic energy builds up (Shibata and Magara 2011) and in a sudden outbreak accelerates charged particles (mostly electrons) in the solar atmosphere which then interact with the surrounding plasma and produce line emission, i.a. in the gamma region, such that it can be measured by INTEGRAL (Wang et al. 2018). Time-correlated to this, so-called *coronal mass ejections* (CMEs) take place. That means, that $10^{12} - 10^{13}$ kg of solar matter are spontaneously being ejected at velocities of up to 2000 $\frac{km}{s}$. Although a time-correlation between the two events exist, a causal relation has not yet been shown (Hanslmeier 2014).

As Figure 4.6 (a) shows, solar flares are measured at timescales of hundreds of seconds. It is expected to measure a broad spectrum of energies, including characteristic lines corresponding to nuclear reactions, as can bee seen in Figure 4.6 (b).

4.4 Gamma-Ray Bursts

Gamma Ray Bursts (GRBs) have first been observed in 1969 (Klebesadel, Strong, and Olson 1973). GRBs are spontaneous outbreaks of great amounts of energy in the range of γ-radiation, i.e. between 20 and 100 keV. They originate in all possible directions and last for several milliseconds to several minutes. The origin for this sudden energy outbreak has not yet been fully understood, but there is several theories as to where the GRBs come from, how they are produced and what possible progenitors for GRBs there are (Hanslmeier 2014). GRBs are generally classified into short-duration GRBs,

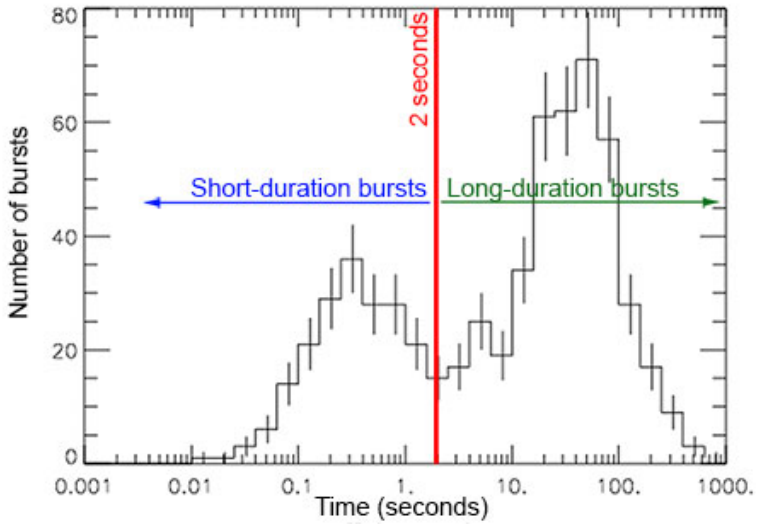

Figure 4.7: Graph of the duration time versus number of bursts for the gamma-ray bursts observed by the BATSE instrument on the Compton Gamma-ray telescope. From NASA 2018a.

which last up to 2s, and long-duration GRBs, which last longer than that. The long type makes up around two thirds of all observed GRBs. (Taylor 2005) The plot in figure 4.7 shows the number of GRBs observed with BATSE (*Burst and Transition Source Experiment*) on board CGRO (*Compton Gamma Ray Observatory*) as a function of duration. From the plot, a classification in short and long GRBs at the threshold of ∼2s is visible as there are two peaks in the distribution.

In many observed events, the duration of the bursts were associated with a specific region of origin, which is why the classification also plays a role in the search for GRB progenitors. Long-duration GRBs are commonly believed to have their origin in high energetic CCSNe (Hjorth 2003). One model is the so-called *Collapsar model*, which involves a star collapsing into a neutron star, surrounded by a massive disc, from which it then quickly accretes matter and collapses into a BH. This BH then interacts with the disc in a way that is not yet fully understood, by which energy is emitted in the form of γ-radiation (Woosley and Bloom 2006; Taylor 2005; MacFadyen, Woosley, and Heger 2001).

Short-duration GRBs tend to occur in greater distance to their galactic nuclei, meaning they most likely do not stem from stars of very high mass (Levan et al. 2008). Instead, following new observations, it is believed that short-duration GRBs have their origin in the collision and merger of two neutron stars. This suggestion is made because of the registration of a short-

duration GRB 2 seconnds after recording a gravitational wave on August 17^{th} (Lipunov et al. 2018).

5 Data Analysis

The most appropriate way to extract information out of a dataset is to fit a model, e.g. a physical expectation oa a process, to the data. This can be a simple function, like a polynomial or a Gaussian, or it can be the extraction of certain parameters from an underlying theory that is supposed to fit the given data. These functions are subject to parameters, describing different assumptions, states or conditions of the model. These parameters are then analyzed as to which value provides the best fit to the data. Thus, when the model is known, the adjustment process is generally a minimization problem in multiple dimensions, because the parameters may influence each other (Press et al. 1992).

5.1 Chi-square Fitting

5.1.1 General Principle

One common way to do this is the Least Squares Method. Since, even if the model used is 100% correct, the data still underlies statistical fluctuations, a tested model will never *exactly* fit the real given data. Therefore, whenever a model is fitted, one tries to find the model parameters, such that the model is closest to the given data. One way to do this, is minimizing the distances of the model to the data, which is done by the *least squares method*. Assuming a model with M adjustable parameters a_j, where $j = 1, ..., M$ to be fitted to a dataset of N points (x_i, y_i), where $i = 1, ..., N$. The aim then is to find the model function

$$y(x) = y(x; a_1, ..., a_M) \tag{6}$$

such that the difference between model and data is as low as possible, or

$$\Delta^2 = \sum_{i=1}^{N} [y_i - y(x_i; a_1, ..., a_M)]^2 \tag{7}$$

is minimized. If considered that every point i in the given data has its own uncertainty σ_i (e.g. its statistical error), one can weigh each data point with its significance, such that equation (7) turns into

$$\chi^2 = \sum_{i=1}^{N} \left(\frac{y_i - y(x_i; a_1, ..., a_M)}{\sigma_i} \right)^2 . \tag{8}$$

Equation (8) is called the Chi-square function. When fitting a known model to data, it is the first approach to minimize the χ^2-function to find the model parameters that best fit the data. If the model is linear, the maximum-likelihood-value equals the minimum-χ^2-value. Therefore this method is called *maximum likelihood estimation.* (Press et al. 1992) To solve it, one has to look into the partial parameter derivatives that shall equal zero and solve the obtained system of equations:

$$0 = \sum_{i=1}^{N} \left(\frac{y_i - y(x_i)}{\sigma_i^2} \right) \left(\frac{\partial y(x_i; ...a_k...)}{\partial a_k} \right) \qquad k = 1, ..., M \tag{9}$$

When more parameters are introduced into a model, the fit will naturally get better. If, for instance, a set of 10 datapoints is given, one could get a perfect fit by using a model with 10 parameters. This model will most likely have nothing to do with what actually happens though - the fit then is over-interpreted, so the information gained out of it is useless in terms of describing the physical background (Press et al. 1992).

That is why the χ^2 is not only important as a value that needs to be minimized - it can also generally be taken as a measure for the goodness of the fit. To find a comparable quantity to compare different models, we introduce the reduced χ^2_{red} which is scaled with the *degrees of freedom* (dof $= N - M$):

$$\chi^2_{red} = \frac{\chi^2}{\text{dof}} \tag{10}$$

A good model should always evolve around $\chi^2 \approx 1$ (Press et al. 1992).

5.1.2 Numerical Methods

For functions with linear parameters the optimization problem is straightforward, but it can get problematic for fits whose parameters are not linear. Because most of the time, there is no existing analytic solution for those problems, numeric approximations have to be used (Press et al. 1992). One such approximation algorithm is based on the steepest descent method. Given a set of parameters, that have to be guessed, the algorithm uses the gradient of the χ^2 function to proceed towards its local minimum and to find reasonable values for the fit parameters. This procedure can be done by an IDL (*Interactive Data Language*) with a function called *CURVEFIT*.

To circumvent the problem of CURVEFIT getting stuck in local minima of the χ^2-function, a Monte-Carlo Markov-Chain (MCMC) is also applied to the data. In a MCMC the parameters have certain prior parameters that are Gaussian distributed. It then performs "random jumps" around the guessed parameters according to the GAussian distribution in parameter

space, to find lower values for χ^2. It therefore can be less accurate than the curvefit function, but it has the ability at its disposal to "tunnel" through local maxima in the χ^2 function.

5.2 Bayesian Blocks

To not rely on a given model too much or if no model to describe the physical process is available, one can use Bayesian statistics to obtain information from a set of data. Scargle 1998 introduced an algorithm that uses Bayesian statistics to extract information from a set of data by segmenting raw counting data into the most probable subsegments, wherein the count rates stay perceptibly constant and has no significant statistical variations. These segments are then called *Bayesian Blocks* (Scargle 1998). With this method, he tries to overcome the common practice of using time bins to extract information from photon counting data, because through binning, a considerable amount of information can get lost by averaging over a bin (Scargle 1998).

The algorithm is based on Bayes' theorem, which can be written as

$$P(\theta|D,M) = \frac{P(D|\theta,M)P(\theta|M)}{P(D|M)}, \tag{11}$$

where D is the data and M is the model containing parameter θ. $P(\theta|D,M)$ herein is the *posterior probability density* of θ, $P(D|M)$ the *prior predictive probability* for the data, $P(D|\theta,M)$ the likelihood for the parameter θ and $P(\theta|M)$ the *prior probability* of parameter θ. All these are to be considered *given the model M*. $P(\theta|D,M)$ can be used to quantify the model's goodness of fit (Scargle 1998).

The main tool used when generating Bayesian Blocks is the comparison between two models and deciding which one is more probable. One key comparison herein is choosing between a model M_1 stating a constant count rate over the observation time T and a model M_2 with two subintervals $T_1 + T_2 = T$ with constant but possibly different count rates (Scargle 1998).

When two models are to be compared, one has to calculate the probability for a model being correct, given the data and the "background information" used. Also following Bayes' theorem, this can be done by (Scargle 1998)

$$P(M_k, |D,I) = \frac{P(D|M_k,I)P(M_k|I)}{P(D|I)}, \tag{12}$$

where M_k names the model k and I sums up all background information, that no further attention will be paid to, because it does not change and therefor has no influence on the calculation. To compare two models j and

k, one can use the *odds ratio* (Scargle 1998)

$$\frac{P(M_k|D)}{P(M_j|D)} = \frac{P(D|M_k)P(M_k)}{P(D|M_j)P(M_j)}. \tag{13}$$

Because $P(D|M_k)$ can be obtained by integrating equation (11) over θ, one receives

$$\rho = \frac{P(M_k|D)}{P(M_j|D)} = \frac{\int P(D|\theta_k, M_k)P(\theta_k|M_k)d\theta_k}{\int P(D|\theta_j, M_j)P(\theta_j|M_j)d\theta_j} \frac{P(M_k)}{P(M_j)}. \tag{14}$$

The quantity of interest when comparing models is therefore

$$J(M_k, D) = P(M_k) \cdot \int P(D|\theta_k, M_k)P(\theta_k|M_K)d\theta_k, \tag{15}$$

wherein the integral

$$\mathcal{L}(M_k, D) = \int P(D|\theta_k, M_k)P(\theta_k|M_K)d\theta_k \tag{16}$$

is defined as the *global likelihood*.

The model for which J becomes greatest is the most likely to be correct - thus the decision between models can be made based on whether the odds ratio ρ is greater or smaller than 1 (Scargle 1998).

As described above, the algorithm described herein is based on deciding between the following two models:

1. A constant Poisson rate
2. Two subsegments with different rates and a changepoint in between

Firstly, the evidence of a constant Poisson Rate Model needs to be established. To do so, the Count rate shall be defined as λ and the time of observation as T. The observation time shall be divided into equal, fixed subintervals δt and k shall be the number of counts retrieved in the Poisson Counting Process (PCP) in an interval δt and therefor be Poisson distributed: (Scargle 1998)

$$P(k|PCP, \Lambda) = \frac{\Lambda^k e^{-\Lambda}}{k!} \tag{17}$$

with $\Lambda = \lambda\delta t$.

If considered, that the Ge detectors of SPI measure single events, thereby allowing highest time resolution, the raw detector data processed contains a set of photon arrival times (Scargle 1998).

$$D = \{t_n, \quad n = 1, 2, ..., N\} \tag{18}$$

In practice, these times do of course have a finite time resolution due to detector dead times. These are not treated as ordinary bins though, because the time intervals are very short compared to astrophysical time scales and the actual number of photons is not recorded, but only whether one or more photons have arrived (Scargle 1998). For SPI these time bins would be $\delta t = 102.4\mu s$ (Vedrenne et al. 2003). Thus the data is still considered *bin free*; the intervals δt shall be called "ticks" (Scargle 1998).

Each tick now receives an integer index m, such that

$$t_m = m\delta t, \tag{19}$$

where $T = M\delta t, m = 1, 2, ..., M$ and the data consists of N indices, one for each photon:

$$D = \{m_n, \quad n = 1, 2, ..., N\}, \tag{20}$$

meaning that photon n is detected at time $m_n\delta t$.

In general, the measurement is treated as a Bernoulli experiment, where we consider two possible outcomes for observable X_m:

$$D : X_m = \begin{cases} 0 & \text{no photons during tick } m \\ 1 & \text{otherwise} \end{cases} \tag{21}$$

with the probabilities

$$\begin{aligned} P(X_m = 0|\Lambda) &= p_0 = e^{-\lambda\delta t} = e^{-\Lambda} \\ P(X_m = 1|\Lambda) &= p_1 = 1 - p_0 = 1 - e^{-\Lambda}. \end{aligned} \tag{22}$$

Thus, with $M_1(\Lambda, T)$ as the Poisson process over T with rate Λ per tick, we get

$$P(D|M_1(\Lambda, T)) = \prod_{m=1}^{M} P(X_m|\Lambda) = p_1^N(1 - p_1)^{M-N}. \tag{23}$$

To now obtain the global likelihood $\mathcal{L} = \int P(D|M_1(p_1))P(p_1|M_1)dp_1$ we need to find the prior $\int P(p_1|M_1)dp_1$ which we get from

$$P(p_1|M_1) = \begin{cases} 1 & \text{for } 0 \leq p_1 \leq 1 \\ 0 & \text{otherwise} \end{cases} \Rightarrow \int P(p_1|M_1)dp_1 = 1. \tag{24}$$

Now we need to integrate

$$\mathcal{L} = \int P(D|M_1(p_1))P(p_1|M_1)dp_1 = \int_0^1 p_1^N(1-p_1)^{M-N}dp_1 = B(N+1, M-N+1), \tag{25}$$

where the *beta function* B can be written in terms of the gamma-function

$$B(x,y) = \frac{\Gamma(x)\Gamma(y)}{\Gamma(x+y)}, \tag{26}$$

which gives us the global likelihood for the single rate model:

$$\mathcal{L}(M_1|D) = \phi(N,M) = \frac{\Gamma(N+1)\Gamma(M-N+1)}{\Gamma(M+2)} = \frac{N!(M-N)!}{(M+1)!} \tag{27}$$

This likelihood depends only on the length of the interval and the number of photons in it (Scargle 1998).

To calculate the alternative model with two different rates and a *changepoint*, we can use the fact that the likelihood of the single rate model only depends on M and N. Because we can assume the two subsegments to be independent from each other, we can calculate the likelihood of the segmented model to be the product of the likelihoods for two separate single rate models. To do so, we take a changepoint index n_{cp} and split the observation time in two intervals with constant count rates. n_{cp} marks the index of the last photon to be measured before the changepoint. Therefore, by splitting up the observation time we obtain four new values for N and M, where (Scargle 1998)

$$\begin{aligned} N_1 &= n_{cp}; \\ N_2 &= N - N_1 = N - n_{cp}; \\ M_1 &= m_{n_{cp}}; \\ M_2 &= M - M_1 = M - m_{n_{cp}}. \end{aligned} \tag{28}$$

From the independence of the two rates we obtain the likelihood ψ of the segmented model to be

$$\psi(n_{cp}) = \phi(N_1, M_1)\phi(N_2, M_2). \tag{29}$$

To decide between the models, we now calculate the odds ratio according to equation (14) to be

$$\mathcal{O}_{21} = \frac{J(M_2|D)}{J(M_1|D)}. \tag{30}$$

If the odds ratio favors the segmented model, equation (29) can be used to calculate the most probable changepoint, thus, the n_{cp} for which $\psi(n_{cp})$ is maximized (Scargle 1998).

To obtain multiple changepoints now, one can use an iterative method to find the most probable segmentation. The iteration is started with the complete dataset, and by the algorithm described above - if in favor of segmenting - two subsegments are produced. For each individual subsegment

the odds ratio is calculated again and - if in favor of segmentation - each subsegment gets segmented once more. The algorithm stops, when for all created subsegments, the constant Poisson rate model is favored over the segmentation (Scargle 1998).

Because in large datasets often the computed odds ratio is greater than 1 by only a small amount, leading to segmentation decisions which due to the little difference in likelihoods are wrong about half of the time. To protect the algorithm against such mistakes, two approaches can be taken. First, chosen segments may tend to only hold very few photons counts - therefore one can introduce a minimum photon number per segment, to avoid such decisions. The second possible approach is to define a prior odds ratio greater than 1, which is then the threshold for a segmentation decision - thus the dataset is only segmented, if the odds ratio is *strongly* in favor of segmentation (Scargle 1998). Both approaches have been used in the following. To apply the above described methods, the MatLab Code samples in Scargle 1998's appendices have been "translated" into IDL code to take out the computations.

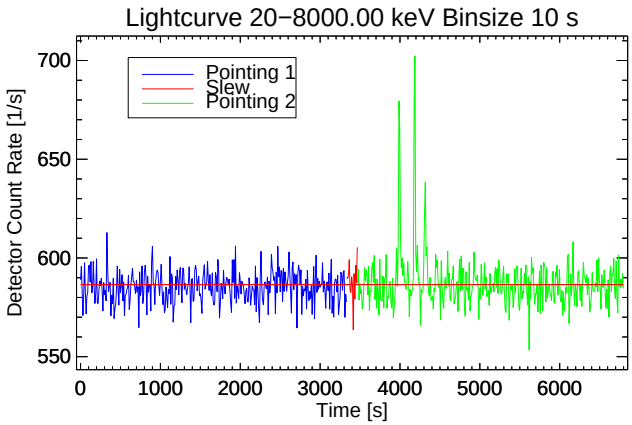

Figure 6.1: The light curve for Pointing 108500320010 (blue), 108500330010 (green) and Slew 108500320021 (red) in between, with time bins of 10s, covering SPI's complete energy range (20 keV - 8 MeV). The straight red line constitutes the average detector count rate.

6 Application of the Methods

Since 2002, INTEGRAL has measured quite a lot of data. In typical analyses of SPI data, it has been a common approach, to look at a pointing as a whole, averaging over the observation time to look for signals on a timescale in the magnitude of several pointings, because much integration time is needed to see signals with a considerable significance. The approach taken for this thesis aimed for finding signals on small timescales within single pointings. To do so, an example has been carried out in two pointings, one of which looks unspectacular at first sight (Pointing 1 in Figure 6.1), while in the pointing after, fluctuations were visible by eye (Pointing 2 in Figure 6.1).

6.1 Gamma-Ray Lightcurves from SPI

To state an example, two Pointings and the slew between them have been observed with respect to their light curves, as can be seen in Figure 6.1. The red, vertical line in the plot marks the average count rate over both pointings and the slew in between. In this plot one can see by eye, that there are three peaks in the second pointing, that at first sight look considerably significant. Yet, by averaging over the time range of $\sim$ 6700s, the count rate

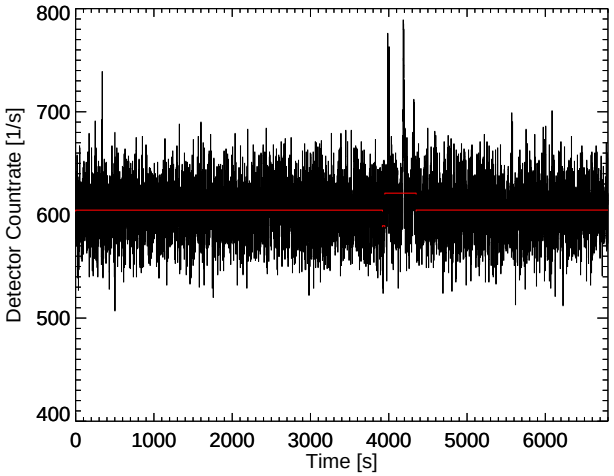

Figure 6.2: The lightcurve as shown in Figure 6.1 with 1s time bins. Starting time is the beginning of the first pointing. The segmentation by Bayesian blocks can be seen in red. The threshold for the segmentation was 1000 photons per segment.

shown by the red line does not seem to be influenced too much by the peaks in Pointing 2. When looking at several pointings and their average count rates at once, one may probably consider the small change in count rates as statistical fluctuation and therefor not significant, which leads to the signal getting lost over averaging.

One approach to look for such fluctuations is the *Bayesian Blocks* algorithm that has been described above.

6.2 Bayesian Blocks

The Bayesian Blocks algorithm has been applied to the light curve in Figure 6.1. In a first approach, when looking at the complete data sample, the change in count rates could be found by the Bayesian Blocks algorithm, as can be seen in Figure 6.2, yet the three different peaks seen by the eye could not be identified. Reason for this is the large threshold of photons per segment which considers the three peaks as only one "outlier".

An attempt to resolve the individual peaks is to "zoom" into the segment with higher count rate that was found by the algorithm and to apply it once more with a lower photon threshold. The result is shown in Figure 6.3.

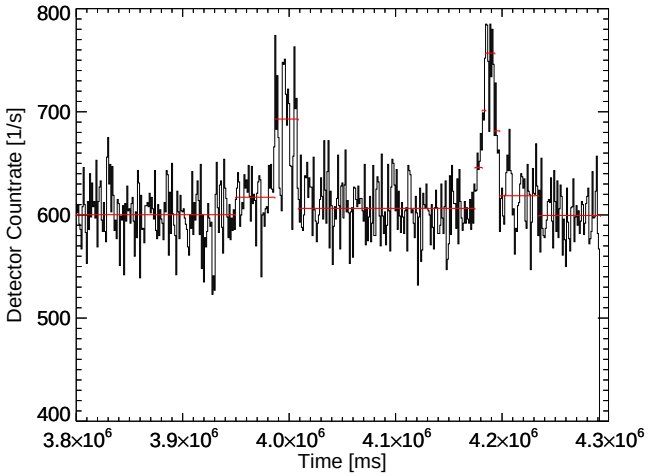

Figure 6.3: The lightcurve for the high countrate segment as seen in Figure 6.2. Time 0 again is the beginning of Pointing 1. In red the Bayesian Blocks can be seen.

Now the individual peaks are clearly identified by the Bayesian Blocks algorithm.

The data shown in the light curves above have included events from all energies within SPI's energy range. In order to identify, in which energy range the current signal was most significant, the lightcurves for different energy bins were also analyzed. Of particular interest were the energy band between 20 and 100 keV, because that is the expected energy domain for GRBs. Moreover, the energy band between 500 and 520 keV has been analyzed, because for Novae a strong signal is expected at 511 keV. To find possible further nucleosynthesis processes from other transients, the energy band from 7 to 8 MeV has also been inspected. Figure 6.4 shows the light curves for the energy bands of (a) 500 - 520 keV and (b) 7 - 8 MeV and Figure 6.5 shows the energy band from 20 to 100 keV. While in Figure 6.4 (a) and (b) no segments have been found by the algorithm, in Figure 6.5 and therefore in the energy band 20 - 100 keV every individual peak is being identified. Thus the background from the other energy bands seems to blurs the signal which is the reason why in Figure 6.2 the individual peaks could not be identified.

From the plots mentioned above the differentiation in energy bands seems to be a reasonable approach to find the significant changepoints in the data sample. These changepoints are then used for a spectral analysis of the

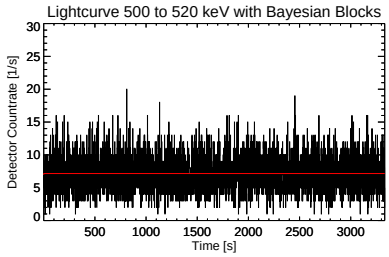

(a) The light curve in the energy band of 500 - 520 keV.

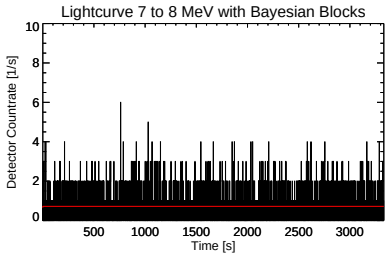

(b) The light curve in the energy band of 7 - 8 MeV.

Figure 6.4: For specific energy bands, the light curves look different. As seen in red, the Bayesian Block Algorithm did not find any significant signals in the energy bands shown above.

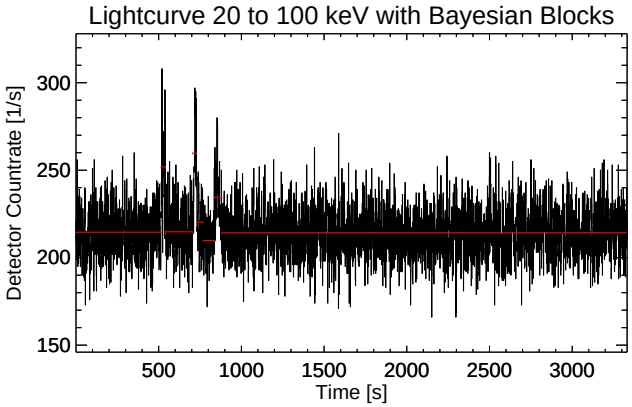

Figure 6.5: Lightcurve for the energy band 20 - 100 keV.

	Peak 1	**Peak 2**	**Peak 3**	**Sum**
$A[s^{-1}cm^{-2}keV^{-1}]$	$0.011 \pm 2 \cdot 10^{-5}$	$0.01 \pm 4 \cdot 10^{-5}$	0.009	0.01 ± 0.0003
α	-0.397 ± 0.133	-0.470 ± 0.120	-1.465	-0.851 ± 0.087
$E_p[keV]$	164.022 ± 36.195	182.326 ± 41.321	504.066	253.838 ± 55.731
χ^2	20.76496700	28.23761100	29.13714700	20.13021600
χ^2_{red}	0.76907284	1.04583740	1.07915360	0.74556354

Table 6.1: The spectral fit parameters obtained from *CURVEFIT*. The relative errors obtained for Peak 3 are in the magnitude of $\frac{\text{error}}{\text{value}} \approx 10^{-10}$ which is why they have not been taken into account here.

signal which will be described in the following.

6.3 Spectral Analysis

To obtain the spectra of the lightcurve peaks seen in Figure 6.5, the background needs to be investigated as well. To do so, a histogram over the energies to the left of the first and to the right of the last peak has been created. The energy binsizes of the histograms have been chosen to be logarithmic as the countrate of SPI drops with increasing energy. Corresponding histograms with the same logarithmic bins have been created for all three peaks individually. By subtracting the background from each individual histogram, a first-order estimate of the signal spectrum is obtained. This has then been normalized with respect to the time range it covers, size of the bins used (which changes, since the bins are logarithmic) and the effective area A_{eff} which depends on the photon energy. A_{eff} was received from the SPI ground calibration (Attie et al. 2003).

For each of the received peak spectra a function has been fitted, which, according to the literature (Mereghetti et al. 2011), is supposed to be a power law with exponential cutoff, described by the following fit function:

$$f(x) = A \cdot \left(\frac{x}{E_0}\right)^{\alpha} \cdot e^{-\frac{x}{E_p}} \tag{31}$$

where E_0 is a normalizing parameter and has been fixed at 25 keV. The red lines in Figure 6.6 show the fitted functions for the spectra according to equation (31). To obtain information about the fit parameters, the fit has been performed with both procedures described above - CURVEFIT and MCMC. The results for the fit parameters A, α and E_p are shown in Table 6.1 for the CURVEFIT analysis and in Table 6.2 for the tsmcmc method. Because of the considerably good time resolution of the three burst-like structures as seen in Figure 6.5, one can also observe the evolution of the spectral fit parameters in time. To do so, all parameters have been plotted

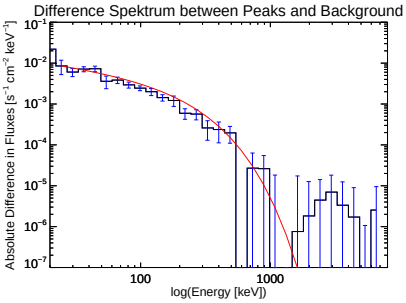

(a) The spectrum of the first Peak with the fitted function.

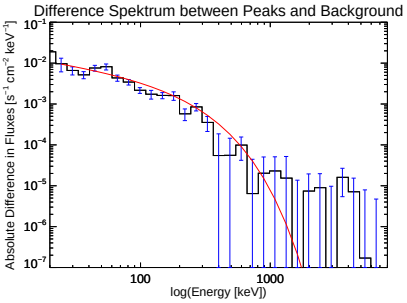

(b) The spectrum of the second Peak with the fitted function.

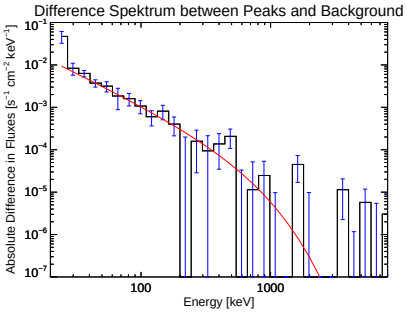

(c) The spectrum of the third Peak with the fitted function.

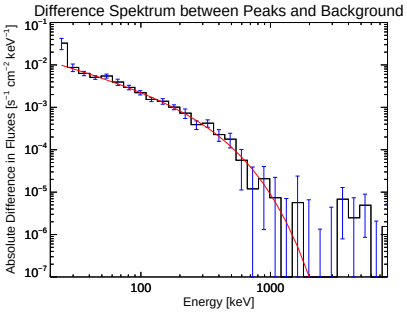

(d) The mean over all three peaks with the fitted function.

Figure 6.6: Spectral Analysis for the Burst Peaks using the *CURVEFIT*-procedure. The error bars have been obtained by Poisson statistic. The signal and background measurement have been treated individually, so the errors have been calculated by the Gaussian propagation of uncertainty. The red line is the fitted model according to equation (31).

	Peak 1	**Peak 2**	**Peak 3**	**Sum**
$A[s^{-1}cm^{-2}keV^{-1}]$	0.011 ± 0.001	0.011 ± 0.001	0.012 ± 0.002	0.011 ± 0.001
α	-0.550 ± 0.159	-0.545 ± 0.175	-1.649 ± 0.145	-0.876 ± 0.097
$E_p[keV]$	185.638 ± 48.843	202.134 ± 69.939	613.696 ± 199.592	261.883 ± 51.236
χ^2	19.657701	28.05725500	27.29000000	20.06175600
χ^2_{red}	0.81907086	1.1690523	1.1370851	0.8359065

Table 6.2: The spectral fit parameters obtained from *MCMC*

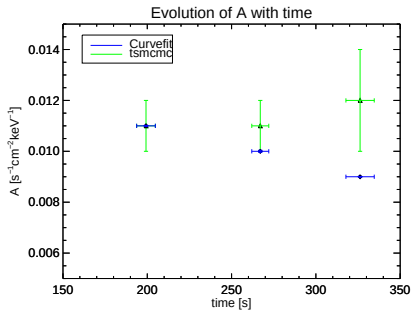

(a) The evolution of the burst amplitude A with time

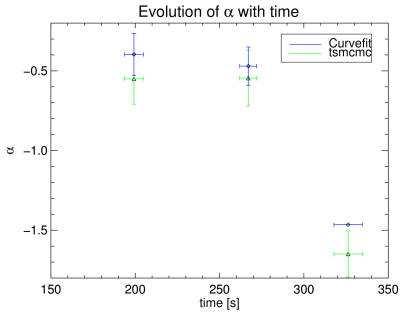

(b) The evolution of the power-law exponent α with time.

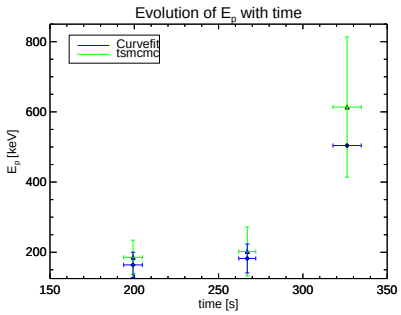

(c) The evolution of the cutoff Energy E_p with time.

Figure 6.7: The time evolution of the fit parameters as fitted according to equation (31). In blue the parameters of the CURVEFIT function are shown, in green one can see the parameters obtained from MCMC. The errors are Gaussian and have been received from the fit.

as a function of time as used in the lightcurves.The resulting plots can be seen in Figure 6.7.

According to the literature (Mereghetti et al. 2011) the object observed is the GRB 110903A that has besides SPI also been located by IBIS and FERMI/GBM on September 3^{rd}, 2011 at 03:54:34 GMT. It is therein stated that the fit function (31) is best used for fitting the spectrum of said GRB. The literature values for the fit parameters compared to the values we found are:

For the literature fit, the integrated spectrum over T_0 to $(T_0 + 368.896s)$ has been used, therefor averaging over all three peaks in addition to some of the background between the peaks and t background prior to the start of the GRB. Other than that, our fit has only taken into account the peaks

	Literature	**Curvefit**	**MCMC**
$E_p[keV]$	$301(-80, +185)$	254 ± 56	262 ± 51
α	$-0.96(-0.29, +0.37)$	(-0.85 ± 0.09)	(-0.88 ± 0.10)
χ^2	77.8	20.1302	20.0618
χ^2_{red}	0.8841	0.7456	0.8359

Table 6.3: The literature values for the fitted spectrum in comparison to the values received from our fit. The Amplitude A, being only a normalizing constant has not been taken into account here.

themselves, while not using the areas between peaks and subtracting the background prior to the GRB start and past its end. The parameters we obtain for this fit are shown in Tables 6.1 and 6.2 in the column "Sum". Within the error bars, all of our results as well as the values given by the literature correspond to each other.

7 Discussion

The goal of this thesis was finding an automated way to analyze count data with respect to the evolution in short time scales. The method used to do so, is described in section 5.2. As described and shown, one way to deal with the background domination od SPI data is the separation into different energy bands. This separation can then also be used to identify the source - signatures in the 20 - 100 keV band, as have been obtained here, speak for GRBs, while signatures in the 500 - 520 keV band can be a sign for an occurring Nova.

The change points found in the analyzed band can then be used to investigate the complete data sample. The changepoints that have been found within the data sample described herein seem to be consistent with what one might assume by looking at the data sample by eye. This means on the one hand, that the peaks seen from the beginning are indeed significant enough for the Bayesian Blocks Algorithm to find them, and on the other hand it means that the Bayesian Blocks Algorithm seems to be sensitive enough to find the Peaks we were looking for.

To improve the fit we obtained, one can analyze the data with respect to the background. This means, a model for the background (= *background model*) needs to be created, taking into account the statistical fluctuations of the time and energy values in the background, and include them into the fit of the signal. Thereby, the accuracy of the fit can be improved and the time dependence of the fit parameters may be object of further investigation.

The time evolution of our fit parameters as seen in Figure 6.7 extends the observations made and published by Mereghetti et al. 2011. As can be seen in the plots, the third and last peak of GRB110903A differs from the first two spectra considerably. Also in the light curve in Figure 6.5 a somewhat broader and less hard intensity flow can be spotted. It is yet to be determined whether this is specific to this GRB, or whether there is other GRBs with a similar time evolutionary structure. In general, from past observations one would expect the spectral parameters to develop in the opposite direction. Prior investigation have shown the cutoff energy to evolve from "hard to soft" which in this context means a change from higher to lower cutoff energies (Chakrabarti et al. 2018).

With the algorithm introduced by Scargle 1998 and applied to the detector counting data of INTEGRAL/SPI, great amounts of data can be analyzed automatically to find similar structures in the SPI Germanium detector data. A perspective for future works on this topic may be the analysis of these datasets and the search for similar structures to the GRB considered in this thesis.

Conclusively we can say, that the Bayesian Blocks algorithm introduced in section 5.2 returns the expected results, making it possible to search for fluctuations on comparably short timescales and analyze their spectral evolution. Thus, it is applicable to the specific problems faced in high-energy astrophysics.

References

Attie, D. et al. (2003). "INTEGRAL/SPI ground calibration". In: *Astronomy & Astrophysics* 411.1, pp. L71–L79. DOI: 10.1051/0004-6361:20031302.

Bode, Michael F. and Aneurin Evans (May 11, 2012). *Classical Novae, 2nd Edition*. CAMBRIDGE UNIV PRESS. 398 pp. ISBN: 1107405343. URL: https://www.ebook.de/de/product/19118703/classical_novae.html.

Bone, Neil (1999). *Observing Meteors, Comets, Supernovae and other Transient Phenomena*. Springer London. DOI: 10.1007/978-1-4471-0579-4.

Brockhaus (2006). *Der Brockhaus Astronomie*. Brockhaus F.A., Mannheim. ISBN: 978-3765312311. URL: https://www.amazon.com/Der-Brockhaus-Astronomie/dp/3765312312?SubscriptionId=0JYN1NVW651KCA56C102&tag=techkie-20&linkCode=xm2&camp=2025&creative=165953&creativeASIN=3765312312.

Chakrabarti, Arundhati et al. (2018). "Spectral evolution of GRBs with negative spectral lag using Fermi GBM observations". In: *Journal of High Energy Astrophysics* 18, pp. 15–20. DOI: 10.1016/j.jheap.2018.01.002.

Courvoisier, Thierry J.-L. (2013). *High Energy Astrophysics*. Chapter 2.1. Springer Berlin Heidelberg. DOI: 10.1007/978-3-642-30970-0.

Diehl, R. et al. (2017). "INTEGRAL/SPI gamma-ray line spectroscopy. Response and background characteristics". In: *Astronomy & Astrophysics*. DOI: 10.1051/0004-6361/201731815.

Diehl, Roland et al. (2015). "SN2014J gamma rays from the 56Ni decay chain". In: *Astronomy & Astrophysics* 574, A72. DOI: 10.1051/0004-6361/201424991.

Dubath, P. et al. (Nov. 2005). "SPI Analysis User Manual". In: *ISDC - INTEGRAL Science Data Centre* 10.2. URL: http://isdc.unige.ch/integral/download/osa/doc/10.2/osa_um_spi.pdf.

Einstein, A. (1905). "Über einen die Erzeugung und Verwandlung des Lichtes betreffenden heuristischen Gesichtspunkt". In: *Annalen der Physik* 322.6, pp. 132–148. DOI: 10.1002/andp.19053220607.

Garcia, R. A. et al. (2007). "Tracking Solar Gravity Modes: The Dynamics of the Solar Core". In: *Science* 316.5831, pp. 1591–1593. DOI: 10.1126/science.1140598.

Garland, Bill (2018). http://www.nuceng.ca/igna/radioactivity.htm. Accessed: April 28th, 2018, 18:18.

Gehrz, Robert D. et al. (1998). "Nucleosynthesis in Classical Novae and its Contribution to the Interstellar Medium". In: *Publications of the Astronomical Society of the Pacific* 110.743, p. 3. URL: http://stacks.iop.org/1538-3873/110/i=743/a=3.

Hanslmeier, Arnold (2014). *Einführung in Astronomie und Astrophysik (Introduction to Astronomy and Astrophysics)*. Springer Berlin Heidelberg. DOI: 10.1007/978-3-642-37700-6.

Hernanz, M. (May 3, 2013). "Gamma-ray emission from nova outbursts". In: *ASP Conference Series* 490, p. 319. arXiv: 1305.0769v1 [astro-ph.HE].

Hjorth, Jens (June 2003). "A very energetic supernova associated with the gamma-ray burst of 29 March 2003". In: *Nature* 423.6942, pp. 847–850. DOI: 10.1038/nature01750.

Janka, Hans-Thomas (2012). "Explosion Mechanisms of Core-Collapse Supernovae". In: *Annual Review of Nuclear and Particle Science* 62.1, pp. 407–451. DOI: 10.1146/annurev-nucl-102711-094901.

Kiener, J. et al. (2005). "Properties of the energetic particle distributions during the October 28, 2003 solar flare from INTEGRAL/SPI observations". In: *Astronomy & Astrophysics* 445.2, pp. 725–733. DOI: 10.1051/0004-6361:20053665.

Kienle, P. and R. E. Segel (1959). "Decay of Co56 and Mn56". In: *Physical Review* 114.6, pp. 1554–1560. DOI: 10.1103/physrev.114.1554.

Klebesadel, Ray W., Ian B. Strong, and Roy A. Olson (1973). "Observations of Gamma-Ray Bursts of Cosmic Origin". In: *The Astrophysical Journal* 182, p. L85. DOI: 10.1086/181225.

Knoll, Glenn F. (2011). *Radiation Detection And Measurement, 4th Edition.* Wiley India. ISBN: 978-0-470-13148-0. URL: https://www.amazon.com/Radiation-Detection-Measurement-4Th/dp/B00A2MXKA8?SubscriptionId=0JYN1NVW651KCA56C102&tag=techkie-20&linkCode=xm2&camp=2025&creative=165953&creativeASIN=B00A2MXKA8.

Kretschmar, P. et al. (2005). "The INTEGRAL mission – an overview". In: *Proceedings of the International Astronomical Union* 1.S230, pp. 59–65. DOI: 10.1017/s1743921306007873.

Kutner, Marc Leslie (July 11, 2003). *Astronomy*. p. 148. Cambridge University Pr. ISBN: 0521529271.

Levan, A. J. et al. (2008). "On the nature of the short-duration GRB 050906". In: *Monthly Notices of the Royal Astronomical Society*. DOI: 10.1111/j.1365-2966.2007.11953.x.

Lipunov, Vladimir et al. (2018). "The discovery of the neutron stars merger GW170817/GRB170817A and a binary stars evolution". In: *New Astronomy* 63, pp. 48–60. DOI: 10.1016/j.newast.2018.02.004.

MacFadyen, A. I., S. E. Woosley, and A. Heger (2001). "Supernovae, Jets, and Collapsars". In: *The Astrophysical Journal* 550.1, pp. 410–425. DOI: 10.1086/319698.

Martin, B. R. and Graham Shaw (1997). *Particle Physics, 2nd Edition*. Wiley. ISBN: 978-0471972853. URL: https://www.amazon.com/Particle-Physics-2nd-B-Martin/dp/0471972851?SubscriptionId=0JYN1NVW651KCA56C102&tag=techkie-20&linkCode=xm2&camp=2025&creative=165953&creativeASIN=0471972851.

Mereghetti, S. et al. (2011). *GRB 110903A: a long GRB detected by INTEGRAL*. https://gcn.gsfc.nasa.gov/gcn/other/110903A.gcn3. Accessed May 8th, 2018, 10:54.

NASA (2018a). https://imagine.gsfc.nasa.gov/Images/science/burst_durations_labelled.jpg. Accessed May 2nd, 2018, 21:03.

– (2018b). *Mass Accretion*. https://www.nasa.gov/images/content/62486main_Making_a_Nova.jpg. Accessed: May 10th, 2018, 20:01.

– (2018c). *The Solar Interior*. https://solarscience.msfc.nasa.gov/interior.shtml. Accessed May 1st, 2018, 18:50.

Panagia, Nino (1985). *Supernovae as Distance Indicators*. Ed. by Norbert Bartel. Springer Berlin Heidelberg. DOI: 10.1007/3-540-15206-7.

– (2000). "SUPERNOVAE". In: *Experimental Physics of Gravitational Waves*. WORLD SCIENTIFIC. DOI: 10.1142/9789812792846_0003.

Piluso, C. J., D. O. Wells, and D. K. McDaniels (1966). "The decay of 56Ni and 57Ni". In: *Nuclear Physics* 77.1, pp. 193–201. DOI: 10.1016/0029-5582(66)90686-9.

Press, William H. et al. (1992). *Numerical Recipes in Fortran 77: The Art of Scientific Computing*. Cambridge University Press. ISBN: 0-521-43064-X.

Roepke, F. K. (Apr. 14, 2008). "Thermonuclear Supernovae". In: *PoS SUPERNOVA:024,2007*. arXiv: 0804.2147v1 [astro-ph].

Scargle, Jeffrey D. (1998). "Studies in Astronomical Time Series Analysis. V. Bayesian Blocks, a New Method to Analyze Structure in Photon Counting Data". In: *The Astrophysical Journal* 504.1, pp. 405–418. DOI: 10.1086/306064.

Schatzmann, Evry L. (1958). *White Dwarfs*. North Holland Press, Amsterdam.

Shaik, Asif (2018). *Photoelectric Effect*. http://www.physics-and-radio-electronics.com/blog/wp-content/uploads/2016/11/photoelectriceffect.png. Accessed: April 29th, 2018, 14:32.

Shibata, Kazunari and Tetsuya Magara (2011). "Solar Flares: Magnetohydrodynamic Processes". In: *Living Reviews in Solar Physics* 8. DOI: 10.12942/lrsp-2011-6.

Shore, Steven N. (Nov. 14, 2012). "Spectroscopy of Novae – A User's Manual". In: *Astronomical Society of India*. arXiv: 1211.3176v1 [astro-ph.SR].

Siegert, Thomas et al. (Mar. 19, 2018). "Gamma-Ray Observations of Nova Sgr 2015 No. 2 with INTEGRAL". In: *Astronomy & Astrophysics*. arXiv: 1803.06888v1 [astro-ph.HE].

Taylor, Paul A. (Sept. 2005). "Long gamma-ray bursts: (current) theory and observation". In: *RAGtime 6/7: Workshop on black holes and neutron stars*. Ed. by S. Hledík and Z. Stuchlík. Silesian University in Opava, 301 ff.

Vedrenne, G. et al. (2003). "SPI: The spectrometer aboard INTEGRAL". In: *Astronomy & Astrophysics* 411.1, pp. L63–L70. DOI: 10.1051/0004-6361:20031482.

Wang, Jiasheng et al. (2018). "Evolution of Photospheric Flow and Magnetic Fields Associated with the 2015 June 22 M6.5 Flare". In: *The Astrophysical Journal* 853.2, p. 143. DOI: 10.3847/1538-4357/aaa712.

Winkler, C. et al. (2003). "The INTEGRAL mission". In: *Astronomy & Astrophysics* 411.1, pp. L1–L6. DOI: 10.1051/0004-6361:20031288.

Witte, C. (2018). *CNO-Cycle*. https://commons.wikimedia.org/w/index.php?curid=3029732. Accessed: April 29th, 18:52.

Woosley, S. E. and J. S. Bloom (2006). "The Supernova - Gamma-Ray Burst Connection". In: *Annual Review of Astronomy and Astrophysics* 44.1, pp. 507–556. DOI: 10.1146/annurev.astro.43.072103.150558.